

## A Theory of the Spring Persistence Barrier on ENSO. Part III: The Role of Tropical Pacific Ocean Heat Content

YISHUAI JIN,<sup>a,b</sup> ZHENGYU LIU,<sup>c</sup> AND MICHAEL J. MCPHADEN<sup>d</sup>

<sup>a</sup> Key Laboratory of Physical Oceanography, Ministry of Education, Ocean University of China, Qingdao, China

<sup>b</sup> Open Studio for Ocean-Climate-Isotope Modeling, Pilot National Laboratory for Marine Science and Technology (Qingdao), Qingdao, China

<sup>c</sup> Atmospheric Science Program, Department of Geography, The Ohio State University, Columbus, Ohio

<sup>d</sup> Pacific Marine Environmental Laboratory, NOAA, Seattle, Washington

(Manuscript received 24 January 2021, in final form 30 July 2021)

**ABSTRACT:** In this paper, we investigate the relationship between upper ocean heat content (OHC) and El Niño–Southern Oscillation (ENSO) sea surface temperature (SST) anomalies mainly using the neutral recharge oscillator (NRO) model both analytically and numerically. Previous studies showed that spring OHC, which leads SST by 6–12 months, represents a major source of predictability for ENSO. It is suggested that this seasonality is caused by the seasonally varying growth rate in SST anomalies. Moreover, a shortened ENSO period will lead to a reduced SST predictability from OHC, with the most significant decrease occurring in the latter half of the calendar year. The cross-correlation relationship between OHC and ENSO SST anomalies is further identified in the damped and self-excited version of the recharge oscillator model. Finally, we suggest that the seasonal growth rate of ENSO anomalies is the cause of the seasonality in the effectiveness of OHC as a predictor in ENSO forecasting, particularly as it relates to the boreal spring persistence barrier and associated spring predictability barrier. We also explain the shorter lead time between spring OHC and ENSO SST anomalies after the turn of the twenty-first century in terms of the apparent higher frequency of the ENSO period.

**KEYWORDS:** ENSO; Seasonal forecasting; Climate variability; Seasonal cycle

### 1. Introduction

The El Niño–Southern Oscillation (ENSO) phenomenon is the most significant interannual signal of the climate system on Earth (McPhaden et al. 2006; Cai et al. 2018), influencing patterns of weather variability worldwide. Therefore, its predictability has received considerable attention, with one major outstanding problem being the boreal spring persistence barrier (SPB) and the associated spring predictability barrier. This barrier has long been noticed in anomalous tropical Pacific sea surface temperature (SST) (e.g., Niño-3.4; 5°S–5°N, 170°–12°W; McPhaden 2003; Ren et al. 2016), sea level pressure (Troup 1965; Webster and Yang 1992), and rainfall (Walker and Bliss 1932; Wright 1979). Specifically, regardless of the initial month, a damped persistence forecast loses its predictability most rapidly in the following April–June, forming the SPB of ENSO (Fig. 1a; Y. Jin et al. 2020). The SPB also shows a distinct decadal modulation, which may be related to thermal damping associated with background SST change (Fang et al. 2019).

Previous studies suggested that ENSO is predictable up to three seasons in advance, based on slow evolution of upper ocean heat content (OHC; Latif et al. 1998). Meinen and McPhaden (2000) found that OHC leads ENSO SST anomalies in the eastern Pacific by 6–7 months. Anderson (2007) found that

subsurface temperature anomalies in the western equatorial Pacific during the boreal summer/fall tend to lead mature ENSO conditions by 12–15 months.

This OHC shows a distinct seasonality of the effectiveness in ENSO prediction. McPhaden (2003) demonstrated that initialization of upper OHC variations may lead to seasonally varying enhancement of ENSO forecasting skill, with the most significant enhancements for forecasts starting in the boreal spring. That is to say, ENSO models often show improvements in forecast skill across the SPB when initialized with observed variations in upper OHC (Smith 1995; Xue et al. 2000). Although the in-phase correlation of Niño-3.4 and OHC is small (lead time = 0 months), especially in the first six calendar months, cross-correlation above 0.6 is found for spring anomalies in OHC leading Niño-3.4 by 7–12 months (Fig. 1b; the 95% significance level is 0.41 for 20 years of data). On the other hand, persistent spring SST anomalies show no skill for such long lead times (Fig. 1a). This point can be further identified in Fig. 1c, which shows the difference between cross-correlation (between OHC and Niño-3.4; Fig. 1b) and the Niño-3.4 autocorrelation (Fig. 1a). For early to late spring, OHC is an effective long lead predictor of ENSO SST anomalies (lead time is more than 6 months; the difference is higher than 0.4 at 6 months lead time in Fig. 1c); however, from summer to autumn, persistent SST anomalies show a higher skill in predicting winter Niño-3.4 anomalies (lead time is about 3–5 months; the difference is negative in Fig. 1c) compared with using OHC. As such, OHC anomalies in the spring can be employed to predict the peak SST anomalies.

Recent studies have found a twenty-first-century phase shift in the relationship between OHC and ENSO SST anomalies such that OHC anomalies in the spring are less effective as an

 Denotes content that is immediately available upon publication as open access.

Corresponding authors: Yishuai Jin, jinyishuai@126.com; Zhengyu Liu, liu.7022@osu.edu

DOI: 10.1175/JCLI-D-21-0070.1

© 2021 American Meteorological Society. For information regarding reuse of this content and general copyright information, consult the AMS Copyright Policy ([www.ametsoc.org/PUBSReuseLicenses](http://www.ametsoc.org/PUBSReuseLicenses)).

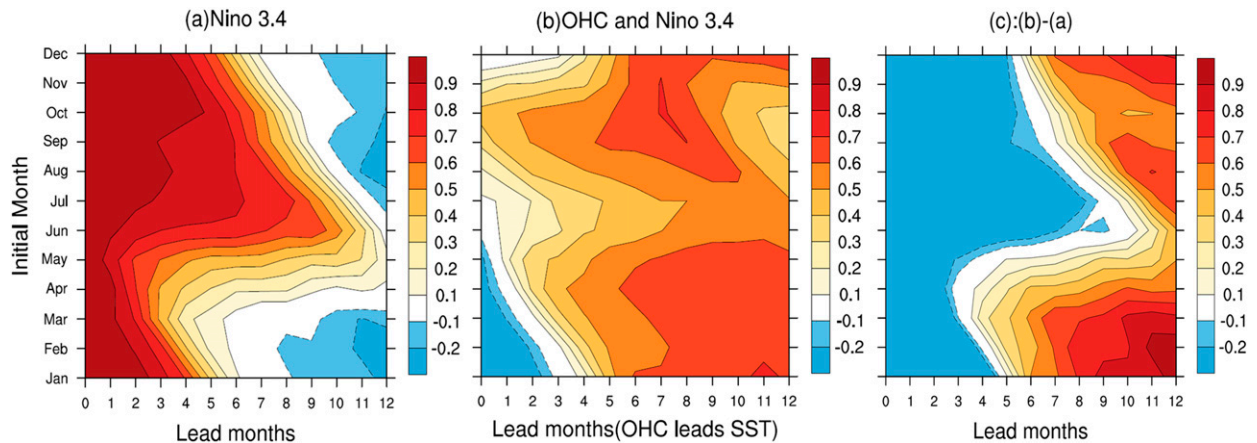


FIG. 1. (a) The autocorrelation of Niño-3.4 SST anomalies for 1980–99 showing persistence as a function of start month. (b) The cross-correlation of OHC and Niño-3.4 SST as a function of start month and lead time for 1980–99. (c) The difference of (b) minus (a).

ENSO SST predictor (McPhaden 2012). Figure 2a shows that this lead time is shifted to only 3–4 months for OHC anomalies in the early to late spring. Another way to see the reduced predictability from OHC is in Fig. 2b: during 1980–99, the cross-correlation between OHC and Niño-3.4 is about 0.6 at 12-month lead time (black solid line in Fig. 2b). However, this cross-correlation is smaller after 2000 with the greatest decrease occurring in the last 6 months of the calendar year (blue solid line in Fig. 2b). The reason for this reduced predictability of ENSO is still under debate. One possible mechanism is that the contribution of the thermocline feedback is decreased (Lai et al. 2018). Considering that OHC plays an important role in ENSO predictability (especially for crossing the SPB) and its effectiveness undergoes decadal modulation, we are interested in the following two questions: 1) How does OHC influence the seasonality of ENSO predictability? 2) What factors may reduce ENSO predictability based on OHC?

The persistence barriers of SST and OHC in the tropical Pacific have been discussed in Part I and Part II of this article (Jin and Liu 2021a,b; hereafter cited as Part I and Part II), respectively. In Part I, we showed how the timing and strength of the SPB depended on ENSO period using analytical and numerical versions of the recharge oscillator model. In Part II, we suggested that the seasonal growth rate of SST anomalies controls persistence barriers in both SST and OHC. Particularly, with the addition of a seasonal SST growth rate in the recharge oscillator model, approximate analytical solutions for the SST and OHC autocorrelation functions demonstrate that the timing of persistence barrier for OHC leads that of SST by a half year and the strength of the two persistence barriers is the same.

Here in Part III we attempt to understand ENSO predictability from OHC mainly in the context of the neutral recharge oscillator (NRO) model. Both analytical and numerical solutions

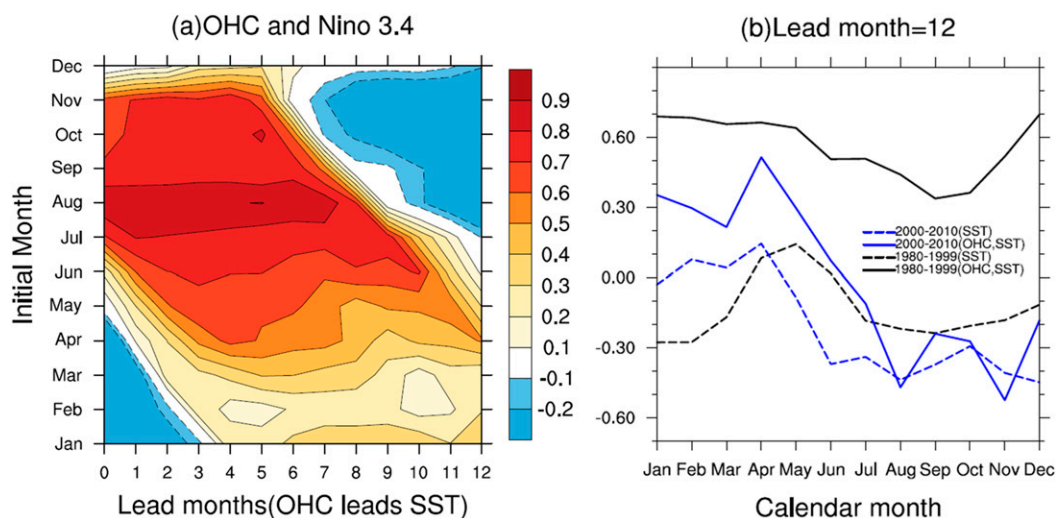


FIG. 2. (a) The cross-correlation of monthly OHC and Niño-3.4 SST anomalies for 2000–10. (b) The cross-correlation with OHC leading SST (solid lines) and autocorrelation of SST (dashed lines) at 12-month lead time during 1980–99 (black lines) and 2000–10 (blue lines).

of the cross-correlation between OHC and SST are derived in the NRO model. These solutions show that with the addition of seasonal growth rate in SST, OHC can improve the predictability of SST at long lead times from the spring initial conditions. This explains why accurate initialization of OHC in ENSO forecast models often reduces the SST spring predictability barrier. We will also show how a shorter ENSO period is associated with a reduced lead time of OHC from the spring as observed after the start of the twenty-first century.

The paper is arranged as follows. The recharge oscillator model and the reanalysis data we use are presented in section 2. In sections 3 and 4, we explore the cross-correlation between OHC and SST in the NRO model in analytical and numerical solutions, respectively. This cross-correlation relationship will also be identified in the damped and self-excited recharge oscillator model in section 5. In section 6, we interpret the observations in the light of these modeled cross-correlation relationships. A summary and discussion are given in section 7.

## 2. Model and data

### a. The parametric recharge oscillator model

Our ENSO model is based upon the recharge oscillator model (Jin 1997a,b), which describes the relationship between variations in OHC and SST anomalies (Meinen and McPhaden 2000). It contains cubic nonlinearity, quadratic nonlinearity, and stochastic noise forcing. This recharge oscillator captures the dynamic relationship between the equatorial Pacific thermocline (or OHC) anomaly ( $H$ ) and eastern equatorial Pacific SST anomaly ( $T$ ) and can be written as follows (Chen and Jin 2020):

$$\frac{dT}{dt} = -\lambda(t)T + \omega_0 H + \sigma\xi - cT^3 + bT^2, \quad (2.1)$$

$$\frac{dH}{dt} = -\omega_0 T, \quad (2.2)$$

$$\frac{d\xi}{dt} = -d\xi + w(t). \quad (2.3)$$

Here,  $\lambda$  is the damping rate (or  $-\lambda$  the growth rate) of the SST anomaly with  $\lambda(t) = R_0 + \lambda_0 \sin(\omega_A t)$  varying seasonally in the annual frequency  $\omega_A = (2\pi/12) \text{ month}^{-1}$ , which leads to the phase locking of ENSO variance (Chen and Jin 2020) and SPB (Levine and McPhaden 2015). The ENSO linear frequency is  $\omega_0$ ;  $w(t)$  is white noise,  $\xi$  is red noise with a decay time scale of  $1 \text{ day}^{-1}$ , and  $\sigma$  is the noise amplitude. The quadratic ( $b$ ) and cubic ( $c$ ) nonlinear terms roughly represent nonlinear dynamic heating from both nonlinear advection and upwelling and the effects of ENSO modulation of tropical instability waves (An 2008). Note here that the damping term of OHC is neglected in Eq. (2.2). This is because on seasonal and longer time scales, the changes in OHC are mainly governed by the geostrophic response to the wind stress forcing rather than by the damping of OHC itself (Burgers et al. 2005).

An approximate analytical solution for the cross-correlation function between OHC and SST is obtained from the neutrally

stable, unforced case of the recharge model with  $R_0 = 0$ ,  $\sigma = 0$ ,  $c = 0$ , and  $b = 0$ . Previous studies have shown that the approximate analytical solution of variance in this neutral model is able to explain the seasonal phase locking of ENSO variance (Stein et al. 2014). Here we will derive the corresponding cross-correlation functions and in turn examine ENSO predictability from OHC. The robustness of the NRO model results will then be confirmed numerically in the recharge model in the damped regime with noise forcing ( $R_0 > 0$ ,  $\sigma > 0$ ,  $c = 0$ ,  $b = 0$ ) and the self-excited unstable regime ( $R_0 < 0$ ,  $\sigma = 0$ ,  $c > 0$ ,  $b = 0$ ). All the numerical results are from the last 500 years of 1000 model year simulations. The numerical model equations, Eqs. (2.1)–(2.3), are solved with a time step of 4 h.

### b. Data

Here we use two datasets from January 1980 to December 2010. One is the Hadley Centre Global Sea Ice and Sea Surface Temperature (HadISST;  $1^\circ \times 1^\circ$ ) observational SST dataset version 1.1 (<https://climatedataguide.ucar.edu/climate-data/sst-data-hadisst-v11>) to define general features of the Niño-3.4 SST anomaly for ENSO. The other is for  $20^\circ\text{C}$  ( $Z_{20}$ ) isotherm depth data from the monthly Simple Ocean Data Assimilation (SODA;  $0.5^\circ \times 0.5^\circ$ ; Carton and Giese 2008). The SODA 3.12.2 data are integrated over  $5^\circ\text{S}$ – $5^\circ\text{N}$ ,  $120^\circ\text{E}$ – $80^\circ\text{W}$  (McPhaden 2003) to estimate the depth of  $Z_{20}$ . This depth of  $Z_{20}$  is determined by interpolation of the gridded subsurface temperature. We then use  $Z_{20}$  as a proxy to represent OHC. Monthly OHC and Niño-3.4 index anomalies are computed relative to a mean seasonal period based on a 31-yr (1980–2010) climatology.

## 3. Analytical solution for the NRO model

In this section, the relation between OHC and SST is studied by deriving an approximate analytical solution to the NRO model. For the linear scenario of the NRO model ( $R_0 = 0$ ,  $\sigma = 0$ ,  $c = 0$ ,  $b = 0$ ), an approximate analytical solution of  $T$  can be obtained for a weak annual cycle of the growth rate, or small  $\lambda_e$  [nondimensional number,  $\lambda_e = (\lambda_0/\omega_A) \ll 1$ ]. The autocorrelation of  $T$  can be written  $r_T(m, \tau)$ , where  $m$  denotes calendar month from 1 to 12 (representing January to December) and  $\tau$  is the lag in months. Then, from Part I we have

$$r_T(m, \tau) \approx \cos \omega_0 \tau + 2\lambda_e A \sin \omega_0 \tau \sin \frac{\omega_A \tau}{2} \cos \left( \omega_A m + \frac{\omega_A \tau}{2} \right), \quad (3.1)$$

where  $A = \omega_0 \omega_A / (\omega_A^2 - 4\omega_0^2)$  and  $B = (\omega_A^2 - 2\omega_0^2) / (\omega_A^2 - 4\omega_0^2)$ . According to Eq. (3.1), the relationship between the calendar month ( $m$ ) and the minimum autocorrelation at a specific  $\tau$  can be derived as follows:

$$\omega_A m + \frac{\omega_A \tau}{2} = \pi. \quad (3.2)$$

For  $\tau$  close to 0, the minimum autocorrelation occurs in June ( $m = 6$ ); when  $\tau$  increases, the timing of minimum autocorrelation moves to late winter.

By using the relationship between SST and OHC [Eq. (2.2)], the time series of OHC can be derived as

$$H(t) = \cos(\omega_0 t) + \frac{1}{2} \lambda_\varepsilon \omega_0 \left[ \frac{B-A}{\omega_A + \omega_0} \cos(\omega_A + \omega_0)t - \frac{B+A}{\omega_A - \omega_0} \cos(\omega_A - \omega_0)t \right]. \quad (3.3)$$

Defining  $C_1 = (B-A)/(\omega_A + \omega_0)$ ,  $C_2 = (B+A)/(\omega_A - \omega_0)$ ,  $H$  solutions can be simplified as

$$H(t) = \cos(\omega_0 t) + \frac{1}{2} \lambda_\varepsilon \omega_0 C_1 \cos(\omega_A + \omega_0)t - \frac{1}{2} \lambda_\varepsilon \omega_0 C_2 \cos(\omega_A - \omega_0)t. \quad (3.4)$$

According to Eq. (3.4),  $H$  is controlled by the interaction between the ENSO cycle frequency ( $\omega_0$ ) and the annual cycle ( $\omega_A$ ). This is similar to the combination mode (C-mode) described by Stuecker et al. (2015) in the western Pacific warm pool.

The covariance function  $S_{H,T}(m, \tau)$  can be written as

$$S_{H,T}(m, \tau) \approx \frac{1}{2} \sin \omega_0 \tau - \frac{1}{2} \lambda_\varepsilon A \cos \omega_0 \tau \sin[\omega_A(m + \tau)] + \frac{1}{2} \lambda_\varepsilon B \sin \omega_0 \tau \cos[\omega_A(m + \tau)] + \frac{1}{2} \lambda_\varepsilon \omega_0 \left[ \frac{1}{2} (C_1 - C_2) \cos \omega_A m \sin \omega_0 \tau - \frac{1}{2} (C_1 + C_2) \sin \omega_A m \cos \omega_0 \tau \right] \quad (3.5)$$

with  $\tau > 0$  indicating that  $H$  leads  $T$  by  $\tau$  months. Then the cross-correlation  $r_{H,T}(m, \tau)$  can be derived as (see appendix A)

$$r_{H,T}(m, \tau) \approx \sin \omega_0 \tau - 2 \lambda_\varepsilon A \cos \omega_0 \tau \cos \frac{\omega_A \tau}{2} \sin \left( \omega_A m + \frac{\omega_A \tau}{2} \right). \quad (3.6)$$

Equation (3.6) suggests the reason why the spring OHC affects SST predictability at longer lead times (6–12 months). First, when  $\lambda_\varepsilon = 0$  (i.e., there are no seasonal variations in growth rate), Eq. (3.6) shows that the timing of maximum cross-correlation occurs at 1/4 ENSO period. Thus, OHC is a predictor of ENSO SST at these lead times. However, this solution fails to show the seasonality in the effectiveness of OHC in ENSO forecasting. That is why we add the seasonality in the NRO model. When  $\lambda_\varepsilon$  is larger than 0, according to Eq. (3.6), the relationship between the calendar month and maximum cross-correlation for a specific  $\tau$  can be obtained as

$$\omega_A m + \frac{\omega_A \tau}{2} = \frac{3\pi}{2}. \quad (3.7)$$

When  $\tau$  is small ( $\tau \rightarrow 0$ ), a relatively large cross-correlation occurs in boreal autumn ( $m = 9$ , representing September); when  $\tau$  increases ( $\tau \rightarrow 12$  months), the timing of maximum cross-correlation moves forward into spring ( $m = 3$ , representing March). On the other hand, according to Eq. (3.2), for large lead times (6–12 months), the autocorrelation of  $T$

reaches its minimum in the spring such that OHC is a better predictor of ENSO SST than SST itself at this time of year.

To see why spring OHC is less effective at long lead times (e.g., at 12-month lead times) for some cases (e.g., after the 2000s; McPhaden 2012), we simplify Eq. (3.6) by defining  $m_* = \omega_A m$ ,  $\tau_* = \omega_A \tau$ ,  $\omega_* = \omega_0/\omega_A$  such that Eq. (3.6) can be written as follows:

$$r_{H,T}(m_*, \tau_*) \approx \sin \omega_* \tau_* - 2 \lambda_\varepsilon A \cos \omega_* \tau_* \cos \frac{\tau_*}{2} \sin \left( m_* + \frac{\tau_*}{2} \right). \quad (3.8)$$

Specifically, we use  $\tau = 12$  ( $\tau_* = 2\pi$ ) to understand the modulation in the effectiveness of OHC at long lead times. Taking  $\tau_* = 2\pi$  to Eq. (3.8),  $r_{H,T}(m_*, \pi)$  can be further simplified as

$$r_{H,T}(m_*, 2\pi) \approx \sin(\omega_* \times 2\pi) - 2 \lambda_\varepsilon A \cos(\omega_* \times 2\pi) \sin(m_*). \quad (3.9)$$

The relationship between cross-correlation and ENSO period at long lead times (i.e., 12 months) can be identified in Eq. (3.9). When the ENSO period decreases to biennial (i.e.,  $\omega_*$  increases to 1/2),  $\sin \omega_* \times 2\pi$  [first term on the right-hand side of Eq. (3.9)] becomes smaller, indicating that a reduced ENSO period will decrease the cross-correlation for all calendar months. The second term on the right-hand side of Eq. (3.9) suggests an interaction between the annual frequency and the lower frequency. When  $\omega_*$  increases to 1/2,  $\cos(\omega_* \times 2\pi)$  decreases to  $-1$  and  $-A \cos(\omega_* \times 2\pi)$  increases. Accordingly, for  $0 < m_* < \pi$  (initial month ranges from January to June), as  $\sin(m_*) > 0$ ,  $-2 \lambda_\varepsilon A \cos(\omega_* \times 2\pi) \sin(m_*)$  becomes larger indicating increased predictability. On the other hand, for  $\pi < m_* < 2\pi$  (for initial month from July to December),  $\sin(m_*) < 0$  and  $-2 \lambda_\varepsilon A \cos(\omega_* \times 2\pi) \sin(m_*)$  becomes smaller, implying a loss of predictability. Combining two terms on the right-hand side of Eq. (3.9), a shortened ENSO period will correspond to a reduced predictability from OHC with its greatest decrease in predictability in the last six months of the calendar year.

We have found that with a seasonal growth rate in SST anomalies, OHC is a source of predictability at large lead times (6–12 months) for the boreal winter SST. Moreover, this seasonality of ENSO predictability from OHC is modulated by the period of ENSO. We will further examine these features next through numerical solutions.

#### 4. Numerical solution for the NRO model

In this section, features of the analytical solution derived above are compared to numerical solutions of the NRO model. We first discuss the reason why we can use spring OHC as a predictor for winter SST. When the ENSO period is 2.5 years ( $\omega_0 = \pi/15$  month<sup>-1</sup>) and  $\lambda_\varepsilon = 0.6/\pi$  (Part I), the autocorrelation of SST in the spring decays to zero after a 6–12-month lag (Fig. 3a) in the numerical solution. On the other hand, the cross-correlation between OHC and SST increases to a peak (Fig. 3b) when spring OHC leads SST at these lead times. As such, OHC can be regarded as a predictor of winter SST. The same holds true when ENSO period is lengthened (4 years;  $\omega_0 = \pi/24$  month<sup>-1</sup>,  $\lambda_\varepsilon = 0.6/\pi$ ; Fig. 3b). This result is consistent with Eq. (3.7) and the analytical solution (Fig. A1).

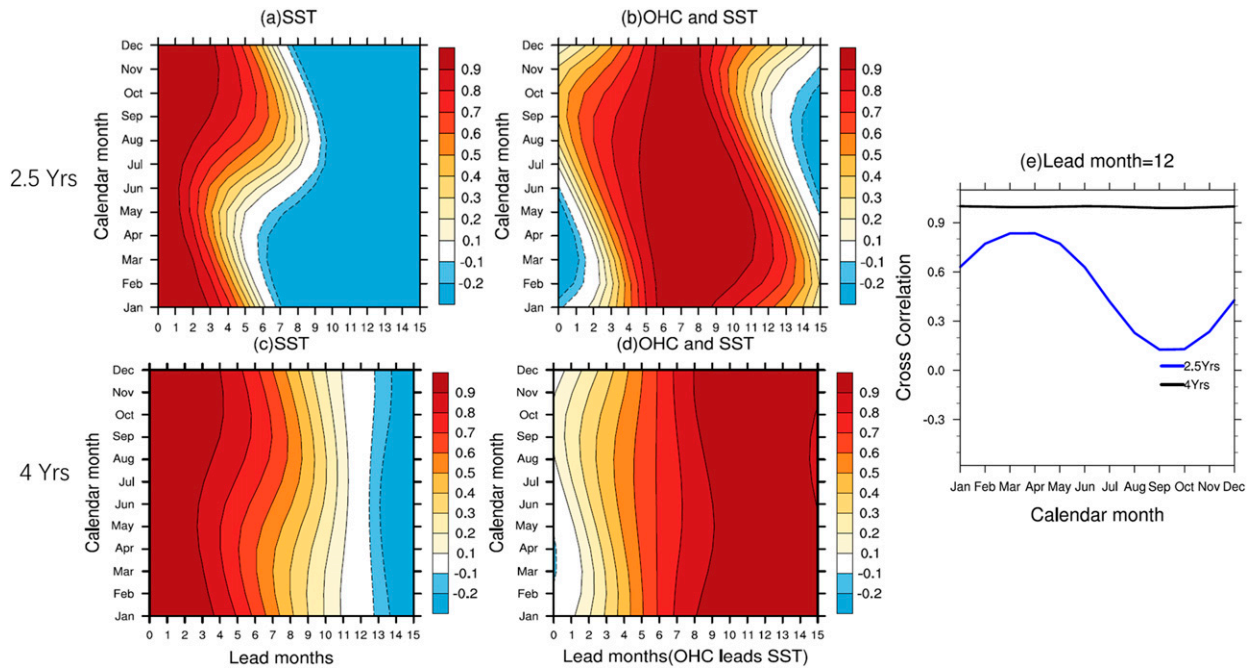


FIG. 3. Numerical solutions for the NRO model. (a) The persistence of SST and (b) the cross-correlation between OHC and SST for ENSO period of 2.5 years ( $\omega_0 = \pi/15 \text{ month}^{-1}$ ). Lead times  $> 0$  indicate that OHC leads SST. (c),(d) As in (a) and (b), but for an ENSO period of 4 years ( $\omega_0 = \pi/24 \text{ month}^{-1}$ ). (e) The cross-correlation at 12-month lead time when the ENSO period is 2.5 years (blue line) and 4 years (black line).

However, spring OHC is less effective as a predictor for winter SST when the ENSO period is shortened (Fig. 3e). When ENSO period is 4 years ( $\omega_0 = \pi/24 \text{ month}^{-1}$ ), the cross-correlation is close to 1 at lead time of 12 months. As  $\omega_0$  increases (i.e., ENSO period is 2.5 years), the cross-correlation between OHC and SST is smaller for all calendar months (blue vs black line in Fig. 3e) at longer lead times (e.g., 12 months). Moreover, this cross-correlation decreases more for autumn

OHC than spring OHC at the same lead time (Fig. 3e). These two features can be identified in the first and second term on the right-hand side of (3.9), respectively.

The role of ENSO period in affecting the cross-correlation at long lead times for all calendar months can be further seen in Fig. 4 for periods ranging from 2.5 to 5 years. The cross-correlation between OHC and SST decreases for all calendar months when ENSO period is shortened to 2.5 years, which is

OHC and SST, Lead month=12

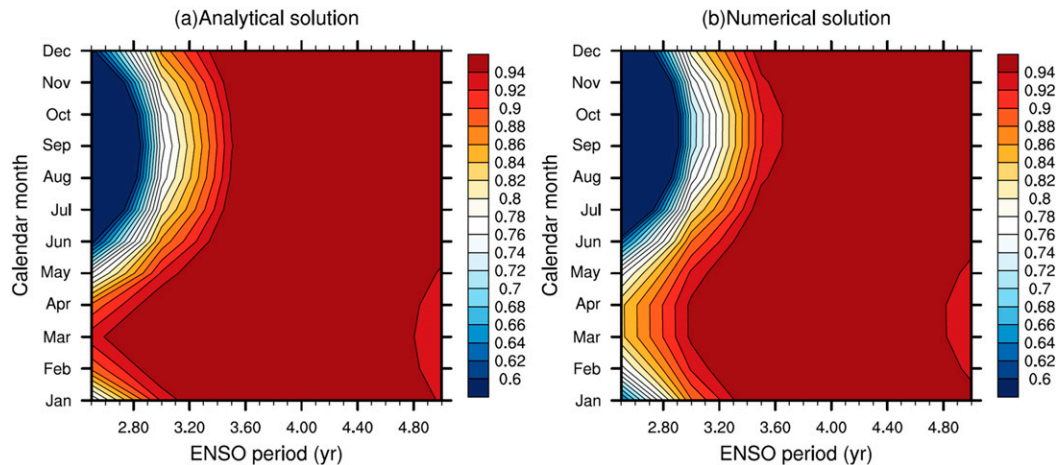


FIG. 4. The cross-correlation at 12-month lead time (OHC leading SST) from the NRO model with  $\lambda_\varepsilon = 0.6/\pi$  for all calendar months when ENSO period ranges from 2.5 to 5 years. (a) Analytical solution and (b) numerical solution.

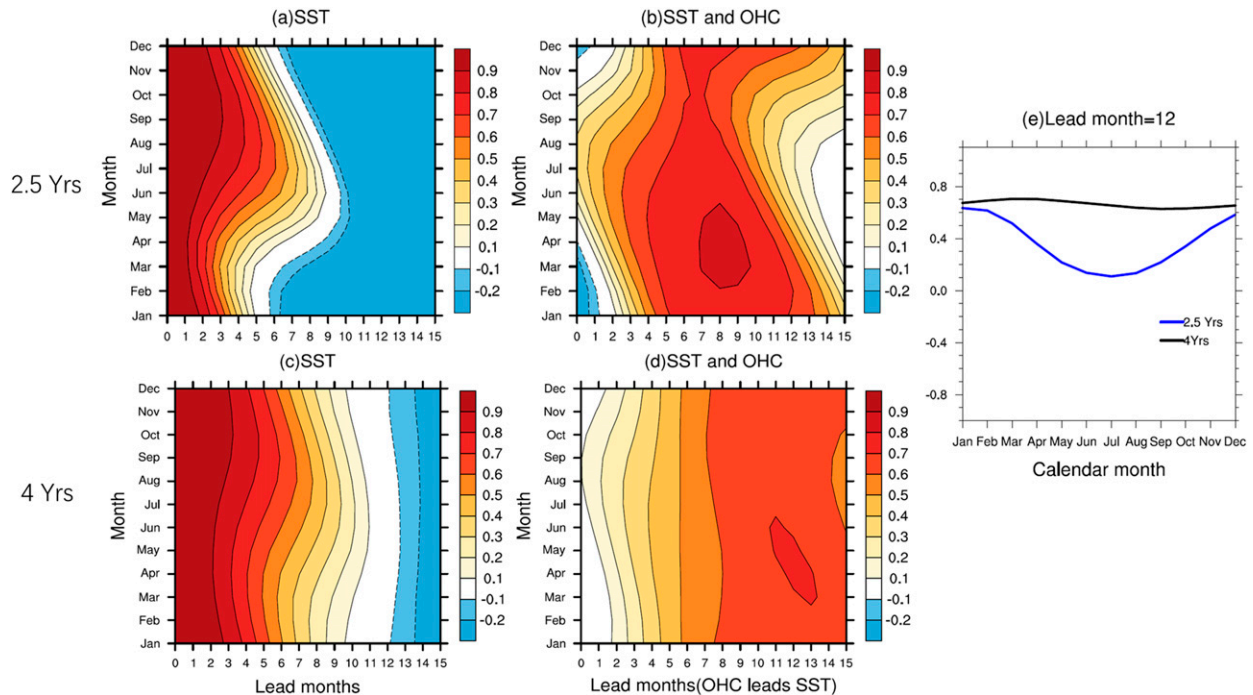


FIG. 5. As in Fig. 3, but for the damped recharge oscillator model.

evident in both the analytical and numerical solutions. However, the cross-correlation decreases much less during the first half of the year compared to the latter half, due to the interaction between the annual frequency and lower ENSO frequency.

In summary, our study of the NRO model here shows that the seasonally varying growth rate is the cause of the seasonality in the effectiveness of OHC as a predictor of ENSO SSTs. When the ENSO period decreases, so too does the effectiveness of spring OHC in ENSO predictability. We note that for these cases without OHC damping the long lead correlations are artificially high in the NRO, but this does not obscure the central issue we address in Fig. 4, which is the frequency dependence of OHC as a predictor of ENSO SST variations. We further explore these relationships in the more complex damped regime ( $R_0 > 0, \sigma > 0, c = 0, b = 0$ ) and self-excited regime ( $R_0 < 0, \sigma = 0, c > 0, b = 0$ ).

## 5. Numerical solutions for damped and self-excited ENSO regimes

### a. Damped regime

Parameters set for the damped regime are (Chen and Jin 2020)  $R_0 = -0.1 \text{ month}^{-1}$ ,  $\lambda_e = 0.6/\pi$ ,  $\sigma = 1/9 \text{ month}^{-1}$ , and  $d = 0.66 \text{ month}^{-1}$ . When the ENSO period  $\omega_0$  is defined as  $\omega_0 = \pi/15 \text{ month}^{-1}$  (i.e., 2.5 years), the autocorrelation of spring SST decays to zero at leads of about 6–12 months (Fig. 5a), while the cross-correlation between OHC and SST reaches its maximum (Fig. 5b). This is also consistent for longer ENSO periods (e.g.,  $\omega_0 = \pi/24 \text{ month}^{-1}$ ; Fig. 5c vs Fig. 5d).

Furthermore, the ENSO period can affect ENSO predictability from OHC at long lead times of, for example, 12 months (Fig. 5e). When the ENSO period is 4 years, the cross-correlation is close to 0.7 at this lead time (black line in Fig. 5e). Note here that, because of the effect of damping, the cross-correlation is smaller than in the NRO model at this lead time. When ENSO period decreases to 2.5 years, the cross-correlation decreases for all calendar months. Moreover, the largest decrease of cross-correlation occurs in July, two months earlier than in the NRO model (Fig. 5e vs Fig. 3e) because of annual mean damping. This annual mean damping will shift the timing of SPB (Liu et al. 2019) as reflected in the cross-correlation. The relationship between ENSO period and cross-correlation at large lead times is further demonstrated in Fig. 6. With the lengthened of ENSO period, the cross-correlation is higher, with the greatest impact of OHC in the latter half of the year.

### b. Self-excited regime

In the self-excited regime, we set the parameters for ENSO as  $R_0 = 0.1 \text{ month}^{-1}$ ,  $c = 1/62.3 \text{ month}^{-1}$ , and  $b = 0$  (Chen and Jin 2020). Here we also set  $\lambda_e = 0.6/\pi$  to be consistent with the damped regime. When  $\omega_0 = \pi/15 \text{ month}^{-1}$  (ENSO period is 2.5 years), a strong persistence barrier is found for SST in the spring (Fig. 7a), while OHC is a significant predictor of SST at 6–12-month lead times (Fig. 7b). A similar feature can be found when ENSO period increases ( $\omega_0 = \pi/24 \text{ month}^{-1}$ ; Fig. 7d).

Moreover, a shortened ENSO period results in OHC in the spring being less effective as a predictor of ENSO SST. When the ENSO period decreases from 4 to 2.5 years, the cross-correlation is reduced, with the greatest decrease occurring late

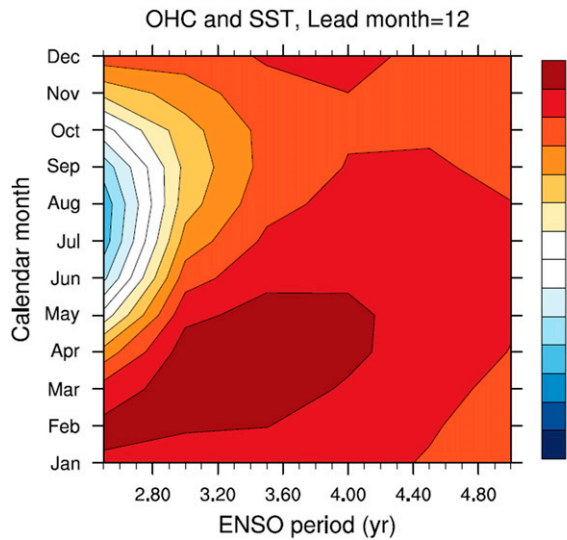


FIG. 6. As in Fig. 4a, but for the damped recharge oscillator model.

in the calendar year (Fig. 7c). This frequency dependence is further illustrated in Fig. 8.

**6. Understanding the relationship between OHC and ENSO SST in observations**

In the previous section, we compared results for two different ENSO regimes with the NRO mode and found consistent robust features that can be used to explain the seasonality of ENSO predictability based on OHC. In particular, the

seasonally varying growth rate of SST anomalies accounts for the strong seasonally varying OHC impact on the predictability of ENSO SST. These results can help us interpret observed variability in the relationship between OHC and ENSO SSTs. For instance, during both 1980–99 and 2000–10, OHC has more influence on the predictability of ENSO SST in the spring compared to the autumn at long (e.g., 12 months) lead times (Figs. 1 and 2). The main reason for this feature is the seasonal cycle of SST growth rate according to our analytical and numerical model solutions. This growth rate is specified in our formulation of the recharge oscillator theory and is controlled by background conditions in the tropical Pacific (Jin et al. 2019) and sensitivity parameters (e.g., the response of wind stress on the SST anomalies; Stein et al. 2014; F.-F. Jin et al. 2020).

Observations also indicate that a shorter ENSO period is related to the reduced predictability from OHC after the twenty-first century (McPhaden 2012). Specifically, for 1980–99, spring OHC led ENSO SST anomalies at lead times up to 12 months with high correlation (Fig. 2). However, after the turn of the twenty-first century, this predictability was reduced (Fig. 2b), with its largest decrease occurring in the last six months of the calendar year. Moreover, five El Niños occur between 1980 and 1999 (at roughly a period of 4 years) versus four between 2000 and 2010 (roughly a period is 2.5 years). Thus El Niño occurred more frequently in the early twenty-first century (McPhaden 2012), with a period shortening from quasi-quadrennial to quasi-biennial after 2000 (see also Wang and Ren 2017). Thus, a shorter ENSO period is related to reduced ENSO predictability based on OHC. Moreover, the interaction of annual cycle and ENSO period variations leads to a greater loss of predictability in the latter half of the calendar year.

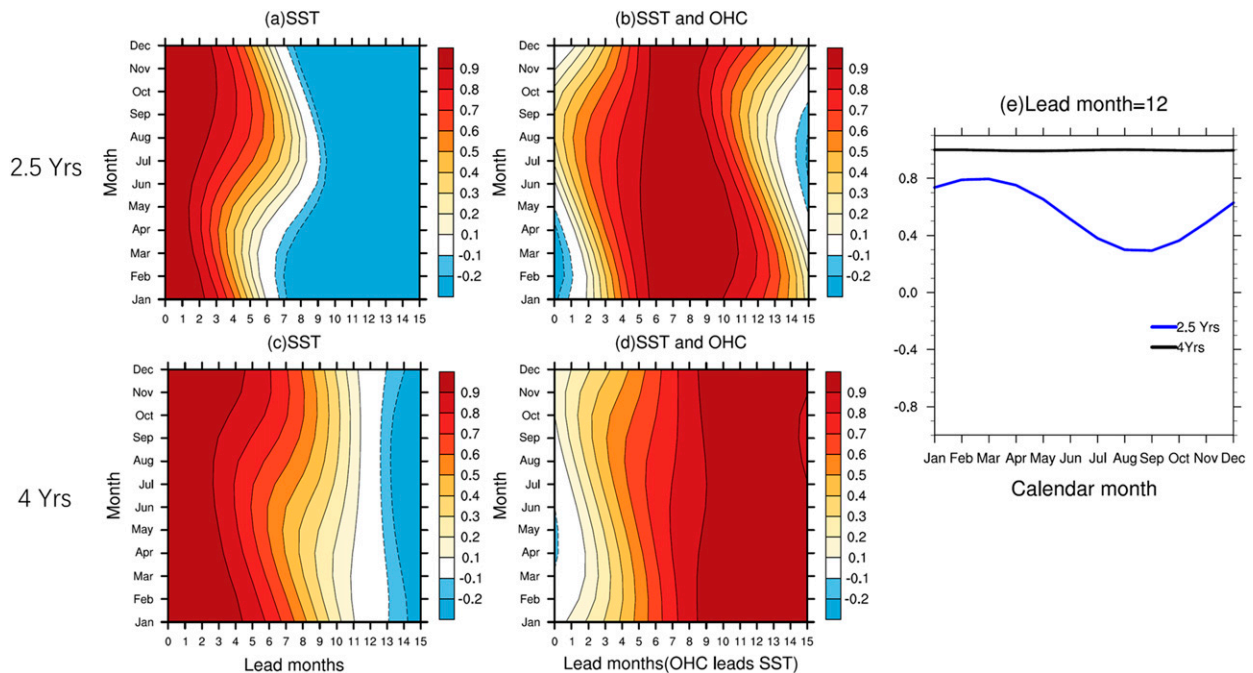


FIG. 7. As in Fig. 5, but for the self-excited recharge oscillator model.

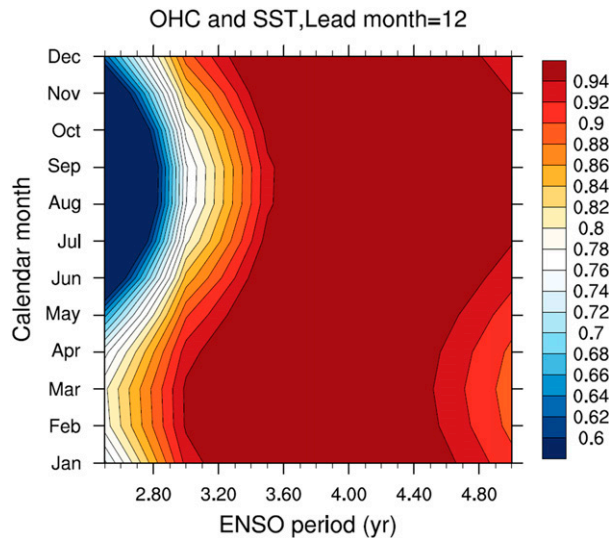


FIG. 8. As in Fig. 6a, but for the self-excited recharge oscillator model.

As noted by McPhaden (2012), the shift toward higher-frequency ENSO events with lower predictability at the turn of the twenty-first century coincides with a shift toward more frequent central Pacific (CP) versus eastern Pacific (EP) El Niño events. The recharge oscillator theory, with only 1 degree of freedom for ENSO SST variability, cannot explicitly represent what we now commonly refer to as ENSO diversity (i.e., ENSO events with different spatial structures and temporal evolution) (Feng et al. 2020; Capotondi et al. 2020). However, our results are consistent with both observations and more complex general circulation models (e.g., Kug et al. 2009) that indicate OHC is less effective as a predictor of CP events than EP events.

## 7. Summary and discussion

This paper attempts to understand the observed relationship between OHC and ENSO SST anomalies using simple theoretical concepts building on recharge oscillator theory. Based on the previous studies indicating that upper OHC in the spring represents a major source of predictability for ENSO SST anomalies at lead times of 6–12 months (Meinen and McPhaden 2000; McPhaden 2003), an analytical solution derived from the NRO model shows that this relationship is based on the seasonal growth rate in SST anomalies. Moreover, the analytical solution suggests that a shortened ENSO period will lead to a decrease of SST predictability from OHC, with the smallest decrease in the first half of the calendar year and the largest decrease in the last half of the calendar year. This differential reduction in predictability is due to the interaction between annual frequency and the lower ENSO frequency. These features are also identified in the numerical solutions to the NRO model and in the damped and self-excited recharge oscillator model formulations. As such, these results indicate that the seasonally varying growth rate explains the seasonality in the effectiveness of OHC as a predictor in ENSO forecast model initialization (Smith et al. 1995). Moreover, the phase shift in the

relationship between OHC and ENSO SST at the start of the twenty-first century (McPhaden 2012) is consistent with a shorter-period ENSO cycle.

The spring persistence barrier and predictability barrier are related but not identical. The spring predictability barrier describes the dramatic drop in prediction skill across the spring for numerical predictions of ENSO. According to the previous studies, the initial errors play an important role in this loss of predictability (Mu et al. 2007; Duan et al. 2009; Duan and Wei 2013; Duan and Hu 2016). On the other hand, seasonal cycle of SST growth rate causes the SPB (Levine and McPhaden 2015; Jin et al. 2019). Specifically, a small growth rate (i.e., a weak coupling between ocean and atmosphere) in the spring leads to the persistence barrier. As a result of this small growth rate, initial errors are more prominent and affect the forecasts more readily compared to other seasons. As such, SPB as a feature of the ENSO life cycle is an indicator of its predictability during the springtime.

Our approach has been to prescribe the frequency of the ENSO cycle in the context of the recharge oscillator theory to examine how ENSO periodicity affects predictability. The question of what causes these changes in period is thus beyond the scope of this study. Lu et al. (2018), however, discuss how thermocline and zonal advective feedbacks, operating within the framework of recharge oscillator dynamics, control ENSO periodicity  $\omega_0$ . Further research on how these competing processes affect ENSO predictability is warranted.

We should also bear in mind that other factors may also affect the relationship between ENSO SST and OHC. According to Lübbecke and McPhaden (2014), the ENSO cycle was not only shorter in the 2000s, but more damped, which would strengthen ENSO SPB (Y. Jin et al. 2020) and in turn, also reduce the lead time for OHC as predicted in our model (more details can be found in solutions to the analytical and numerical solutions of the damped recharge oscillator in appendix B). In addition, other factors such as westerly wind bursts (WWBs), which act as state-dependent noise forcing (Levine and McPhaden 2015) and which have an imprint on OHC itself (Neske and McGregor 2018; Planton et al. 2018), can affect the relationship between SST and OHC anomalies. How to understand the combined effects of these processes on ENSO predictability from OHC requires further study.

*Acknowledgments.* We thank the editor and two anonymous reviewers for their helpful comments on this research. This work is supported by Chinese MOST 2017YFA0603801, NSFC41630527, and U.S. NSF AGS-1656907; it is PMEL contribution 5286.

*Data availability statement.* HadISST v1.1 data can be downloaded online at <https://climatedataguide.ucar.edu/climate-data/sst-data-hadisst-v1.1>. SODA 3.12.2 data can be accessed at <https://dsrs.atmos.umd.edu/DATA/soda3.12.2/REGRIDED/ocean/>.

## APPENDIX A

### Derivation of Cross-Correlation between SST and OHC Based on the NRO Model

The seasonal variance of OHC [ $\sigma_H^2(m)$ ] can be obtained as follows:

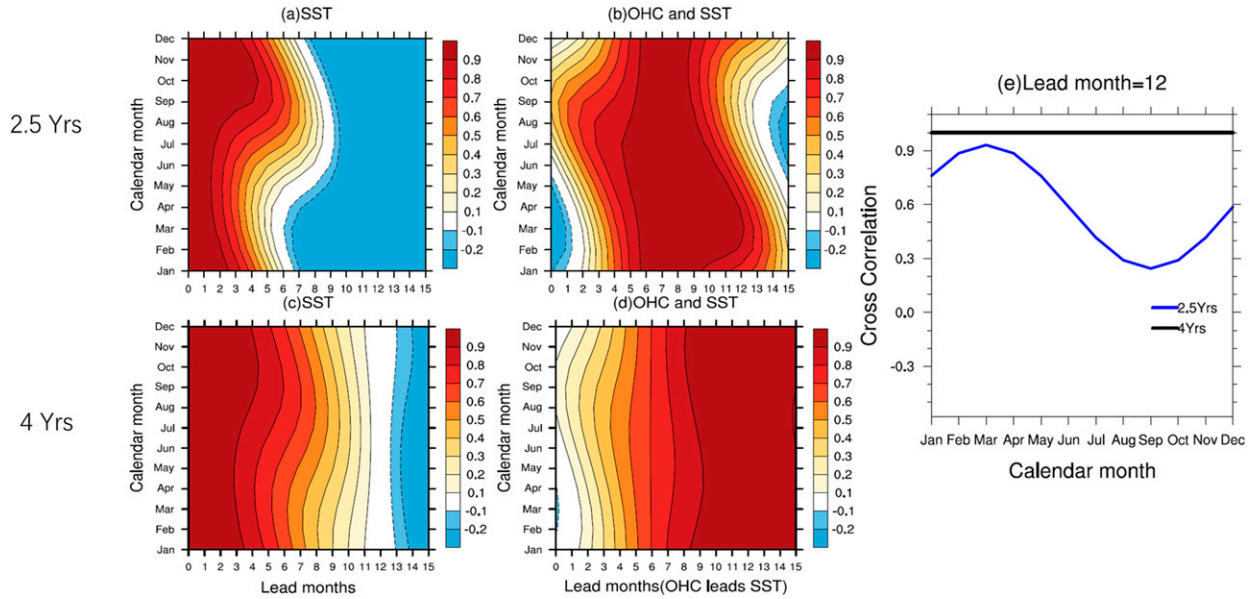


FIG. A1. As in Fig. 3, but for analytical solutions of the NRO model.

$$\sigma_H^2(m) = \frac{1}{2} + \lambda_\varepsilon \omega_0 \left( \cos \omega_A m \times \frac{1}{2} \right) \left( \frac{B-A}{\omega_A + \omega_0} - \frac{A+B}{\omega_A - \omega_0} \right). \tag{A1}$$

As  $A > 0, B > 0, \omega_A > \omega_0 > 0$ , so  $-(A+B)/(\omega_A - \omega_0) + (-A+B)/(\omega_A + \omega_0) < 0$ . The maximum variance of OHC occurs in June ( $m = 6$ ).

As  $C_1 = (B - A)/(\omega_A + \omega_0), C_2 = (A + B)/(\omega_A - \omega_0), C = C_1 - C_2$ , so  $\sigma_H^2(m)$  can be simplified as

$$\sigma_H^2(m) = \frac{1}{2} + \lambda_\varepsilon C \omega_0 \left( \cos \omega_A m \times \frac{1}{2} \right). \tag{A2}$$

By using Eq. (3.5) and Eq. (A2), the cross-correlation between  $H$  and  $T$  can be derived as follows:

$$\begin{aligned} r_{H,T}(m, \tau) &= \frac{S_{H,T}(m, \tau)}{\sqrt{\sigma_H^2(m)\sigma_T^2(m + \tau)}} \\ &\approx \left\{ \frac{1}{2} \sin \omega_0 \tau - \frac{1}{2} \lambda_\varepsilon A \cos \omega_0 \tau \sin[\omega_A(m + \tau)] + \frac{1}{2} \lambda_\varepsilon B \sin \omega_0 \tau \cos[\omega_A(m + \tau)] \right. \\ &\quad \left. + \frac{1}{2} \lambda_\varepsilon \omega_0 \left[ \frac{1}{2} (C_1 - C_2) \cos \omega_A m \sin \omega_0 \tau - \frac{1}{2} (C_1 + C_2) \sin \omega_A m \cos \omega_0 \tau \right] \right\} \\ &\quad \times 2 \left\{ 1 - \frac{1}{2} \lambda_\varepsilon \omega_0 (C_1 - C_2) \cos \omega_A m - \lambda_\varepsilon B \cos[\omega_A(m + \tau)] \right\} \\ &\approx \sin \omega_0 \tau - \lambda_\varepsilon A \cos \omega_0 \tau \sin[\omega_A(m + \tau)] - \frac{1}{2} \lambda_\varepsilon \omega_0 (C_1 + C_2) \sin \omega_A m \cos \omega_0 \tau \end{aligned} \tag{A3}$$

$$C_1 + C_2 = \frac{2\omega_A}{(\omega_A^2 - 4\omega_0^2)}, \quad A = \frac{\omega_0 \omega_A}{\omega_A^2 - 4\omega_0^2}.$$

So,

$$\begin{aligned} r_{H,T}(m, \tau) &= \sin \omega_0 \tau - \lambda_\varepsilon A \cos \omega_0 \tau [\sin \omega_A(m + \tau) + \sin \omega_A m] \\ &= \sin \omega_0 \tau - 2\lambda_\varepsilon A \cos \omega_0 \tau \cos \frac{\omega_A \tau}{2} \sin \left( \omega_A m + \frac{\omega_A \tau}{2} \right) \end{aligned} \tag{A4}$$

The analytical solution, Eq. (A4), captures the major features of the numerical solution (Fig. 3), as shown in Fig. A1. When

$\omega_0 = \pi/15$  and  $\pi/24$  ( $\lambda_\varepsilon = 0.6/\pi$ ), respectively, we can see that the cross-correlation is large for spring OHC at long lead times. These results also indicate that a shorter ENSO period corresponds to a reduced predictability (black vs blue line in Fig. A1e).

## APPENDIX B

### The Role of Damping in the Cross-Correlation between OHC and SST

The damped recharge oscillator model (without seasonally varying in growth rate) can be written as

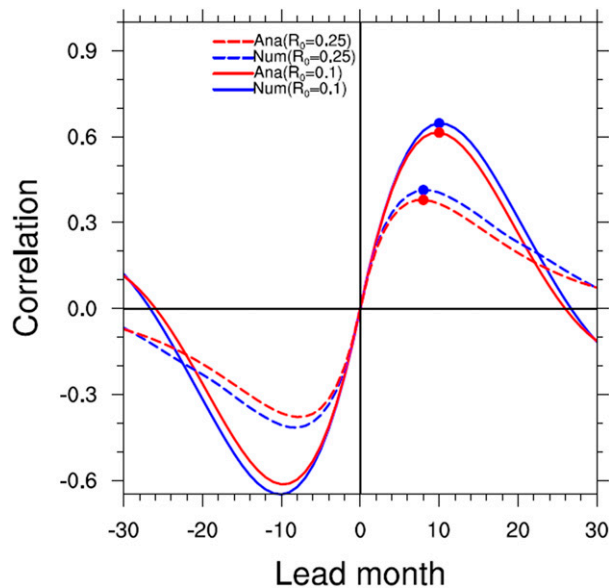


FIG. B1. Cross-correlation between OHC and SST anomalies in the damped recharge oscillator model ( $\omega_0 = \pi/24 \text{ month}^{-1}$ ; ENSO period is 4 years). Blues and red lines are numerical solutions and analytical solutions, respectively. Solid and dashed lines show the cases for  $R_0 = 0.1$  and  $0.25 \text{ month}^{-1}$ , respectively. Circles indicate the timing of the maximum cross-correlation.

$$\frac{dT}{dt} = -R_0 T + \omega_0 H + \xi, \quad (\text{B1})$$

$$\frac{dH}{dt} = -\omega_0 T. \quad (\text{B2})$$

Here,  $R_0$  is annual mean damping rate ( $-R_0$  represents the growth rate). According to the perturbation method (An and Jin 2010), the cross-correlation between SST and OHC ( $\tau > 0$  indicates that OHC leads SST for  $\tau$  month) can be derived analytically as follows:

$$r_{H,T}(\tau) = \frac{e^{-(R_0/2)\tau} \sin \Omega \tau}{\sqrt{1 - \left(\frac{R_0}{2\omega_0}\right)^2}}, \quad (\text{B3})$$

where  $\Omega = \sqrt{\omega_0^2 - (R_0/2)^2}$ .

As  $R_0$  tends to 0, the timing of maximum cross-correlation (MCR) occurs at 1/4 ENSO period. On the other hand, for  $R_0$  close to  $2\omega_0$ ,  $\Omega$  tends to be zero and MCR occurs when  $\tau \rightarrow 0$ . As such, for a larger  $R_0$  (i.e., a more damped system) the lead time between OHC and ENSO SSTs will decrease.

Both analytical and numerical solutions show that a smaller  $R_0$  (i.e., less damped system) will increase the lead time between OHC and SST, as shown in Fig. B1. If we set ENSO to 4 years ( $\omega_0 = \pi/24 \text{ month}^{-1}$ ) with  $R_0 = 0.1 \text{ month}^{-1}$  the MCR occurs at 9 months and is 0.6. When we increase  $R_0$  to  $0.25 \text{ month}^{-1}$ , the MCR is smaller (0.35) and the timing is shortened (8 months). As such, the effectiveness of OHC in ENSO forecasting is reduced as the system becomes more damped.

## REFERENCES

- An, S.-I., 2008: Interannual variations of the tropical ocean instability wave and ENSO. *J. Climate*, **21**, 3680–3686, <https://doi.org/10.1175/2008JCLI1701.1>.
- , and F.-F. Jin, 2010: Linear solutions for the frequency and amplitude modulation of ENSO by the annual period. *Tellus*, **63A**, 238–243, <https://doi.org/10.1111/j.1600-0870.2010.00482.x>.
- Anderson, B. T., 2007: On the joint role of subtropical atmospheric variability and equatorial subsurface heat content anomalies in initiating the onset of ENSO events. *J. Climate*, **20**, 1593–1599, <https://doi.org/10.1175/JCLI4075.1>.
- Burgers, G., F.-F. Jin, and G. J. van Oldenborgh, 2005: The simplest ENSO recharge oscillator. *Geophys. Res. Lett.*, **32**, L13706, <https://doi.org/10.1029/2005GL022951>.
- Cai, W., and Coauthors, 2018: Increased variability of eastern Pacific El Niño under greenhouse warming. *Nature*, **564**, 201–206, <https://doi.org/10.1038/s41586-018-0776-9>.
- Capotondi, A., A. T. Wittenberg, J. S. Kug, K. Takahashi, and M. J. McPhaden, 2020: ENSO diversity. *El Niño Southern Oscillation in a Changing Climate*, *Geophys. Monogr.*, Amer. Geophys. Union, Vol. 253, 65–86.
- Carton, J. A., and B. S. Giese, 2008: A reanalysis of ocean climate using Simple Ocean Data Assimilation (SODA). *Mon. Wea. Rev.*, **136**, 2999–3017, <https://doi.org/10.1175/2007MWR1978.1>.
- Chen, H.-C., and F.-F. Jin, 2020: Fundamental behavior of ENSO phase locking. *J. Climate*, **33**, 1953–1968, <https://doi.org/10.1175/JCLI-D-19-0264.1>.
- Duan, W., and C. Wei, 2013: The ‘spring predictability barrier’ for ENSO predictions and its possible mechanism: Results from a fully coupled model. *Int. J. Climatol.*, **33**, 1280–1292, <https://doi.org/10.1002/joc.3513>.
- , and J. Hu, 2016: The initial errors that induce a significant ‘spring predictability barrier’ for El Niño events and their implications for target observation: Results from an Earth system model. *Climate Dyn.*, **46**, 3599–3615, <https://doi.org/10.1007/s00382-015-2789-5>.
- , X. Liu, K. Zhu, and M. Mu, 2009: Exploring the initial errors that cause a significant ‘spring predictability barrier’ for El Niño events. *J. Geophys. Res. Oceans*, **114**, 114, <https://doi.org/10.1029/2008JC004925>.
- Fang, X. H., F. Zheng, Z. Y. Liu, and J. Zhu, 2019: Decadal modulation of ENSO spring persistence barrier by thermal damping processes in the observation. *Geophys. Res. Lett.*, **46**, 6892–6899, <https://doi.org/10.1029/2019GL082921>.
- Feng, Y., X. Chen, and K.-K. Tung, 2020: ENSO diversity and the recent appearance of central Pacific ENSO. *Climate Dyn.*, **54**, 413–433, <https://doi.org/10.1007/s00382-019-05005-7>.
- Jin, F.-F., 1997a: An equatorial ocean recharge paradigm for ENSO. Part II: A stripped-down coupled model. *J. Atmos. Sci.*, **54**, 830–847, [https://doi.org/10.1175/1520-0469\(1997\)054<0830:AEORPF>2.0.CO;2](https://doi.org/10.1175/1520-0469(1997)054<0830:AEORPF>2.0.CO;2).
- , 1997b: An equatorial ocean recharge paradigm for ENSO. Part I: Conceptual model. *J. Atmos. Sci.*, **54**, 811–829, [https://doi.org/10.1175/1520-0469\(1997\)054<0811:AEORPF>2.0.CO;2](https://doi.org/10.1175/1520-0469(1997)054<0811:AEORPF>2.0.CO;2).
- , and Coauthors, 2020: Simple ENSO models. *El Niño Southern Oscillation in a Changing Climate*, *Geophys. Monogr.*, Amer. Geophys. Union, Vol. 253, 119–151.
- Jin, Y., and Z. Liu, 2021a: A theory of the spring persistence barrier on ENSO. Part I: The role of ENSO period. *J. Climate*, **34**, 2145–2155, <https://doi.org/10.1175/JCLI-D-20-0540.1>.
- , and —, 2021b: A theory of the spring persistence barrier on ENSO. Part II: Persistence barriers in SST and ocean heat content. *J. Climate*, **34**, 5555–5564, <https://doi.org/10.1175/JCLI-D-20-0540.1>.

- , —, Z. Lu, and C. He, 2019: Seasonal period of background in the tropical Pacific as a cause of ENSO spring persistence barrier. *Geophys. Res. Lett.*, **46**, 13 371–13 378, <https://doi.org/10.1029/2019GL085205>.
- , Z. Lu, and Z. Liu, 2020: Controls of spring persistence barrier strength in different ENSO regimes and implications for 21st century changes. *Geophys. Res. Lett.*, **47**, e2020GL088010, <https://doi.org/10.1029/2020GL088010>.
- Kug, J.-S., F.-F. Jin, and S.-I. An, 2009: Two types of El Niño events: Cold tongue El Niño and warm pool El Niño. *J. Climate*, **22**, 1499–1515, <https://doi.org/10.1175/2008JCLI2624.1>.
- Lai, A. W.-C., M. Herzog, and H. F. Graf, 2018: ENSO forecasts near the spring predictability barrier and possible reasons for the recently reduced predictability. *J. Climate*, **31**, 815–838, <https://doi.org/10.1175/JCLI-D-17-0180.1>.
- Latif, M., and Coauthors, 1998: A review of the predictability and prediction of ENSO. *J. Geophys. Res. Oceans*, **103**, 14 375–14 393, <https://doi.org/10.1029/97JC03413>.
- Levine, A. F. Z., and M. J. McPhaden, 2015: The annual period in ENSO growth rate as a cause of the spring predictability barrier. *Geophys. Res. Lett.*, **42**, 5034–5041, <https://doi.org/10.1002/2015GL064309>.
- Liu, Z., Y. Jin, and X. Rong, 2019: A theory for the seasonal predictability barrier: Threshold, timing, and intensity. *J. Climate*, **32**, 423–443, <https://doi.org/10.1175/JCLI-D-18-0383.1>.
- Lu, B., F.-F. Jin, and H.-L. Ren, 2018: A coupled dynamic index for ENSO periodicity. *J. Climate*, **31**, 2361–2376, <https://doi.org/10.1175/JCLI-D-17-0466.1>.
- Lübbecke, J. F., and M. J. McPhaden, 2014: Assessing the 21st century shift in ENSO variability in terms of the Bjerknes stability index. *J. Climate*, **27**, 2577–2587, <https://doi.org/10.1175/JCLI-D-13-00438.1>.
- McPhaden, M. J., 2003: Tropical Pacific Ocean heat content variations and ENSO persistence barriers. *Geophys. Res. Lett.*, **30**, 1480, <https://doi.org/10.1029/2003GL016872>.
- , 2012: A 21st century shift in the relationship between ENSO SST and warm water volume anomalies. *Geophys. Res. Lett.*, **39**, L09706, <https://doi.org/10.1029/2012GL051826>.
- , S. E. Zebiak, and M. H. Glantz, 2006: ENSO as an integrating concept in Earth science. *Science*, **314**, 1740–1745, <https://doi.org/10.1126/science.1132588>.
- Meinen, C. S., and M. J. McPhaden, 2000: Observations of warm water volume changes in the equatorial Pacific and their relationship to El Niño and La Niña. *J. Climate*, **13**, 3551–3559, [https://doi.org/10.1175/1520-0442\(2000\)013<3551:OOWWVC>2.0.CO;2](https://doi.org/10.1175/1520-0442(2000)013<3551:OOWWVC>2.0.CO;2).
- Mu, M., W. Duan, and B. Wang, 2007: Season-dependent dynamics of nonlinear optimal error growth and El Niño–Southern Oscillation predictability in a theoretical model. *J. Geophys. Res.*, **112**, D10113, <https://doi.org/10.1029/2005JD006981>.
- Neske, S., and S. McGregor, 2018: Understanding the warm water volume precursor of ENSO events and its interdecadal variation. *Geophys. Res. Lett.*, **45**, 1577–1585, <https://doi.org/10.1002/2017GL076439>.
- Planton, Y., J. Vialard, E. Guilyardi, M. Lengaigne, and T. Izumo, 2018: Western Pacific oceanic heat content: A better predictor of La Niña than of El Niño. *Geophys. Res. Lett.*, **45**, 9824–9833, <https://doi.org/10.1029/2018GL079341>.
- Ren, H. L., F.-F. Jin, B. Tian, and A. A. Scaife, 2016: Distinct persistence barriers in two types of ENSO. *Geophys. Res. Lett.*, **43**, 10 973–10 979, <https://doi.org/10.1002/2016GL071015>.
- Smith, N. R., 1995: An improved system for tropical ocean subsurface temperature analyses. *J. Atmos. Oceanic Technol.*, **12**, 850–870, [https://doi.org/10.1175/1520-0426\(1995\)012<0850:AISFTO>2.0.CO;2](https://doi.org/10.1175/1520-0426(1995)012<0850:AISFTO>2.0.CO;2).
- Stein, K., A. Timmermann, N. Schneider, F.-F. Jin, and M. F. Stuecker, 2014: ENSO seasonal synchronization theory. *J. Climate*, **27**, 5285–5310, <https://doi.org/10.1175/JCLI-D-13-00525.1>.
- Stuecker, M. F., F.-F. Jin, A. Timmermann, and S. McGregor, 2015: Combination mode dynamics of the anomalous northwest Pacific anticyclone. *J. Climate*, **28**, 1093–1111, <https://doi.org/10.1175/JCLI-D-14-00225.1>.
- Troup, A. J., 1965: The “southern oscillation.” *Quart. J. Roy. Meteor. Soc.*, **91**, 490–506, <https://doi.org/10.1002/qj.49709139009>.
- Walker, G., and E. W. Bliss, 1932: World weather V. *Men. Roy. Meteor. Soc.*, **4**, 53–84.
- Wang, R., and H.-L. Ren, 2017: The linkage between two ENSO types/modes and the interdecadal changes of ENSO around the year 2000. *Atmos. Oceanic Sci. Lett.*, **10**, 168–174, <https://doi.org/10.1080/16742834.2016.1258952>.
- Webster, P. J., and S. Yang, 1992: Monsoon and ENSO: Selectively interactive systems. *Quart. J. Roy. Meteor. Soc.*, **118**, 877–926, <https://doi.org/10.1002/qj.49711850705>.
- Wright, P. B., 1979: Persistence of rainfall anomalies in the central Pacific. *Nature*, **277**, 371–374, <https://doi.org/10.1038/277371a0>.
- Xue, Y., A. Leetmaa, and M. Ji, 2000: ENSO prediction with Markov models: The impact of sea level. *J. Climate*, **13**, 849–871, [https://doi.org/10.1175/1520-0442\(2000\)013<0849:EPWMMT>2.0.CO;2](https://doi.org/10.1175/1520-0442(2000)013<0849:EPWMMT>2.0.CO;2).